ATLAS NOTE

ATLAS-CONF-2011-020

March 24, 2011

A Search for a Light CP-Odd Higgs Boson Decaying to $\mu^+\mu^-$ in ATLAS

The ATLAS Collaboration

Abstract

A search is presented for a very light CP-odd Higgs boson, a_1, decaying to $\mu^+\mu^-$, using pp collisions at $\sqrt{s} = 7$ TeV recorded by the ATLAS detector at the LHC, corresponding to an integrated luminosity[1] of 39.3 pb^{-1}. Such a light Higgs boson is predicted in next-to-minimal extensions of the Supersymmetric Standard Model (NMSSM) designed to solve the μ-term problem of the Minimal Supersymmetric Standard Model (MSSM). Its presence can significantly alter the phenomenology of the MSSM Higgs sector. We set new limits on the production cross section times branching ratio, $\sigma(gg \rightarrow a_1) \cdot BR(a_1 \rightarrow \mu^+\mu^-)$, for a_1 masses of 6 – 9 GeV and 11 – 12 GeV, avoiding the region dominated by the Υ resonances.

---

[1] Revised version, March 24, 2011, to correct an inconsistency in the calculation of the total integrated luminosity. This correction shifts the limits by ~10% with respect to the previous version of this document.

1 Introduction

Supersymmetry (SUSY) provides an elegant solution to the hierarchy problem of the Standard Model (SM), unification of gauge couplings at the GUT scale, and a candidate for dark matter. Although the Minimal Supersymmetric Standard Model (MSSM) has many free parameters resulting from the addition of soft SUSY breaking terms (see, for example Ref. [1] and references therein), it does not cover the full phenomenological range. Furthermore, its μ-term must be fine-tuned to agree with LEP limits on SM-like Higgs bosons decaying to $b\bar{b}$ and $\tau^+\tau^-$ [2].

The Next-to MSSM (NMSSM) solves the μ-term problem by introducing a complex singlet scalar field S. This generates the μ-term as the vacuum expectation value of S through spontaneous symmetry breaking, which allows it naturally to reach the electroweak scale without the fine-tuning required in the MSSM [3]. As a consequence of the added scalar field, the Higgs sector of the NMSSM expands to a total of three CP-even scalars (h_1, h_2, h_3), two CP-odd scalars (a_1, a_2) and two charged scalars (H^+, H^-). If the light CP-odd Higgs boson a_1 has a mass $9.2 < m(a_1) < 12$ GeV, the NMSSM can account for the anomalous muon magnetic moment [4]. A light a_1 may also account for the discrepancy in the ratio of Υ widths $\Gamma(\Upsilon \to \tau^+\tau^-)/\Gamma(\Upsilon \to \mu^+\mu^-)$ between the value measured by the BaBar experiment and the value expected in the SM [5, 6, 7], though agreement on the SM calculation is not universal [8]. Furthermore, the additional neutralino present in the NMSSM provides an extra degree of freedom for satisfying dark matter limits [9].

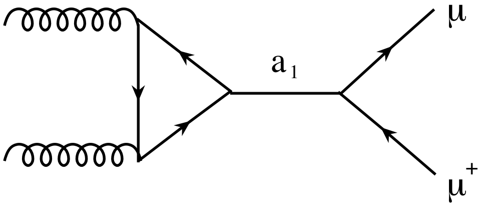

Figure 1: Feynman diagram for $gg \to a_1 \to \mu^+\mu^-$

The additional scalar in the NMSSM can alter MSSM Higgs boson phenomenology dramatically since a light a_1 can open up new decay channels. If the NMSSM decay $h_1 \to 2a_1$ is dominant then standard MSSM and SM search channels ($h \to b\bar{b}$, $WW^\star$, $ZZ^\star$, $\tau^+\tau^-$, $\gamma\gamma$) could miss the Higgs boson, while $H^+ \to a_1 W^+$ would obscure standard charged Higgs boson search modes, $H^+ \to \tau^+\nu, c\bar{s}, t\bar{b}$[1] [10, 11]. Further, if $m(a_1)$ is below the threshold to produce B-hadron pairs ($m(a_1) < 2m_B$) the $h_1 \to 2a_1$ decay allows the h_1 to avoid the LEP lower limit of $m_H \approx$114.4 GeV by suppressing the $b\bar{b}$ channel and also could explain the observed LEP excess in the $\ell^+\ell^- b\bar{b}$ channel near $m_{b\bar{b}} \approx$100 GeV [12]. This mass region is referred to as the *Ideal Higgs* scenario of the NMSSM. In it the preferred a_1 decay channels are $a_1 \to \tau^+\tau^-, c\bar{c}, gg$, and also $a_1 \to \mu^+\mu^-$, $s\bar{s}$ at suppressed levels [10].

Direct a_1 production via gluon fusion ($gg \to a_1$) with a_1 decay to muons ($a_1 \to \mu^+\mu^-$) was considered in Ref. [4]. Two NMSSM parameters are particularly important in this process, which is depicted in Fig. 1. The first is the MSSM parameter $\tan\beta$, the ratio of vacuum expectation values for Higgs doublets giving up-type and down-type fermions mass. The second is specific to the NMSSM: θ_A, which quantifies mixing between the MSSM CP-odd scalar, a_{MSSM}, and the NMSSM CP-odd singlet, a_S:

$$a_1 = \cos\theta_A a_{MSSM} + \sin\theta_A a_S \tag{1}$$

---

[1] Charge conjugate states are implied throughout this note.

Predictions [13] for the branching ratio of $a_1 \to \mu^+\mu^-$ (which is independent of $\cos\theta_A$), and for the $gg \to a_1$ cross section at $\sqrt{s}$=7 TeV (for $\tan\beta$=1, 2, 3, 10 and $\cos\theta_A$=1) vs. a_1 mass are given in Fig. 2(a) and 2(b), respectively. For reference, the predicted value of $\sigma(gg \to a_1) \cdot BR(a_1 \to \mu^+\mu^-)$ at $m(a_1)$=8 GeV with $\tan\beta$=10 and $\cos\theta_A$=0.1 is approximately 3 pb.

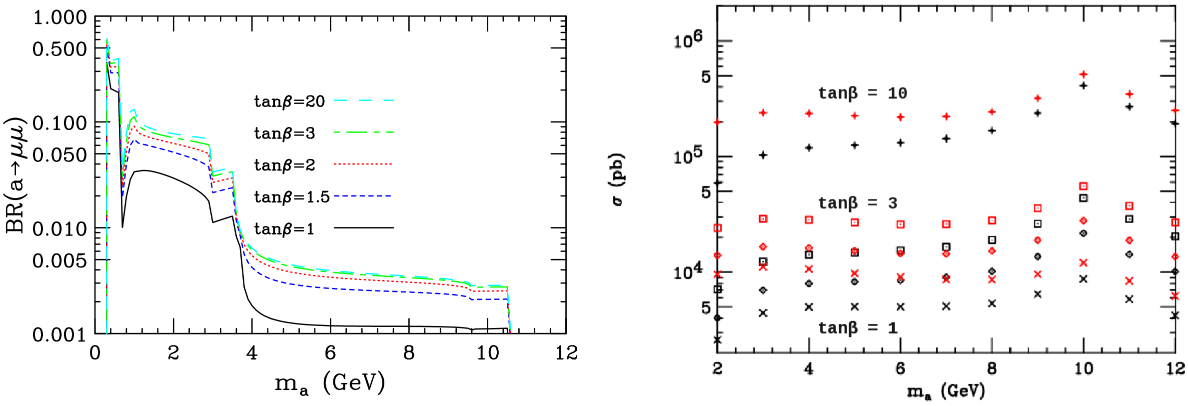

(a)

(b)

Figure 2: (a) Branching ratios for $a_1 \to \mu^+\mu^-$ versus a_1 mass in the Ideal Higgs scenario of the NMSSM. (b) Cross sections for $gg \to a_1$ production vs. a_1 mass at $\sqrt{s}$=7 TeV for $\tan\beta$=1, 2, 3, 10 (from lowest to highest point sets). Black (red) points correspond to cross sections calculated without (with) resolvable parton final state contributions ($gg \to a_1 g$) (taken from Ref. [13]).

In 2009 both the D0 and BaBar experiments published first constraints on the Ideal Higgs scenario. BaBar searched for the radiative transition $\Upsilon \to \gamma a_1$ [14] while D0 searched for $h_1 \to 2a_1 \to 2\mu 2\tau, 4\mu$ [15]. Neither search found any evidence for the a_1, ruling out most scenarios with $m(a_1) < 2m_\tau$ [16] (this conclusion is disputed in Ref. [17]). Recent results from ALEPH [18], searching for Zh production with $h \to 4\tau$ constrain the space $2m_\tau < m(a_1) < 2m_B$, disfavoring NMSSM Ideal Higgs scenarios with $m(a_1)$ not close to $2m_B$ for $\tan\beta \geq 3$. The CDF collaboration also presented preliminary results on a search for $H^+ \to a_1 W^+$ in Ref. [19].

This paper describes a search for a low mass resonance decaying to opposite charge muon pairs in the mass regions 6–9 GeV and 11–12 GeV. Dimuon masses around the Υ resonances (9–11 GeV) are excluded because uncertainties in the expected rate of Υ production make it difficult to distinguish an additional resonance in this mass range. Although the search itself is sensitive to any new particle decaying to muon pairs, exclusion limits are calculated in terms of an NMSSM CP-odd Higgs (a_1), produced through $gg \to a_1$ and with decay to muons, $a_1 \to \mu^+\mu^-$. The primary focus of this search is in the 6–9 GeV region because an a_1 with mass greater than $2m_B$ would decay dominantly to b-quark pairs. The mass region 11–12 GeV is included mainly to explore the mass dependence of our search strategy.

The search may also be complicated by possible mixing of the a_1 with the η_b meson [20, 21, 22]. If present, this would reduce the significance of the result. However, the effect of η_b mixing is not considered in this study.

2 Muon Identification

The ATLAS detector is described in detail in Ref. [23]. Using information from the Inner Detector and the Muon Spectrometer, muons are reconstructed and identified in the region $|\eta| < 2.7$, covering a p_{T} range from 1 GeV to around 1 TeV. Two categories of reconstructed muons are used in this analysis.

1. *Combined* muon reconstruction relies on a statistical combination of track parameters and the covariance matrices of both a standalone Muon Spectrometer (MS) track and an Inner Detector (ID) track, selecting the tracks to be paired on the basis of tight matching criteria to create a combined muon track traversing the ID and MS. Combined reconstruction covers the region $|\eta| < 2.5$.

2. *Tagged* muon reconstruction uses clusters of hits in the MS that are not associated with a combined muon, but which are matched to ID tracks extrapolated to the MS. These muons adopt the measured parameters of the associated ID track, and are reconstructed only up to $|\eta| < 2$, corresponding to the coverage of the Monitored Drift Tubes.

3 Data and Monte Carlo Samples

This analysis uses collision data at a centre-of-mass energy of 7 TeV taken in 2010 corresponding to an integrated luminosity of 39.3 pb^{-1}. Data are only included in this analysis if taken during stable beam LHC running, and in a period when the ATLAS muon spectrometer and inner detector were collecting data of a sufficiently high quality to be suitable for physics analysis. Events are considered for further analysis if they have been selected by a dimuon trigger chain that requires a threshold of 4 GeV for both muons.

Monte Carlo samples for a_1 particles at several masses between 6 and 12 GeV were generated, using the ATLAS MC09 tune [24], with MC@NLO [25] and CTEQ6.6 [26] parton density functions. $\Upsilon(1S)$ MC samples, generated with Pythia 6 [27] and MRST LO* [28] parton density functions, are also used for tests of how well the detector simulation models the data.

Generated events were simulated with Geant4 [29] and fully reconstructed with the same software that was used to process the data from the detector. To speed processing, only those generated events containing two muons with $p_T > 2.5$ GeV and $|\eta| < 2.5$ were passed to the reconstruction. The efficiency of this filter varies from 24% to 58% as the a_1 mass varies from 6.0 to 11.5 GeV. As muon fake rates for the selection described below are found to be small (see Ref. [30]) these filter cuts introduce a negligible bias in the efficiency calculation.

4 Event and Candidate Selection

Selection of $a_1 \to \mu^+\mu^-$ candidates proceeds in two steps. First, events containing a pair of muons with opposite charge consistent with coming from the decay of a single particle are selected. Then, a likelihood-based discriminant is used to reduce combinatoric background and enhance the sensitivity of our search. Each stage of the selection is described in more detail below.

4.1 Dimuon Selection

The dimuon selection follows closely that used in the ATLAS J/ψ and Υ cross-section analyses [31]. Each event is required to pass a trigger requiring two muons with $p_T > 4$ GeV. Events with at least two reconstructed muons are then selected; one of which must be a *combined* muon, and one of which can be classified as either *tagged* or *combined*. The ID track of each muon candidate is required to have at least six Semiconductor Tracker (SCT) hits and one Pixel hit, while both muons must have $|\eta| < 2.5$ and $p_T > 4$ GeV. Both of the muon candidates are required to match the muons that fired the trigger.

All muon pairs in the event with an invariant mass $4.5 < m_{\mu\mu} < 14.0$ GeV[2] that have a good vertex given by the standard fitting algorithm [32] and opposite electric charges are considered. The kinematics

---

[2] This includes sideband regions used in the Likelihood Ratio selection described below.

of these muon pairs are reasonably well described by simulation as can be seen in Fig. 3. In this figure, dimuon p_T and rapidity distributions are shown for the $\Upsilon(1S)$ simulation and for $\Upsilon(1S)$ candidates in data with background subtracted as described in Section 4.2. Also plotted are distributions expected for a_1 resonances of different masses. Differences between the kinematics of the $\Upsilon(1S)$ and a_1 are mainly due to the different production mechanisms for the two particle types. Small discrepancies between data and prediction are expected because the $\Upsilon(1S)$ simulation has not yet been tuned at LHC energies.

The mass spectrum of the selected dimuon candidates is shown in Fig. 4.

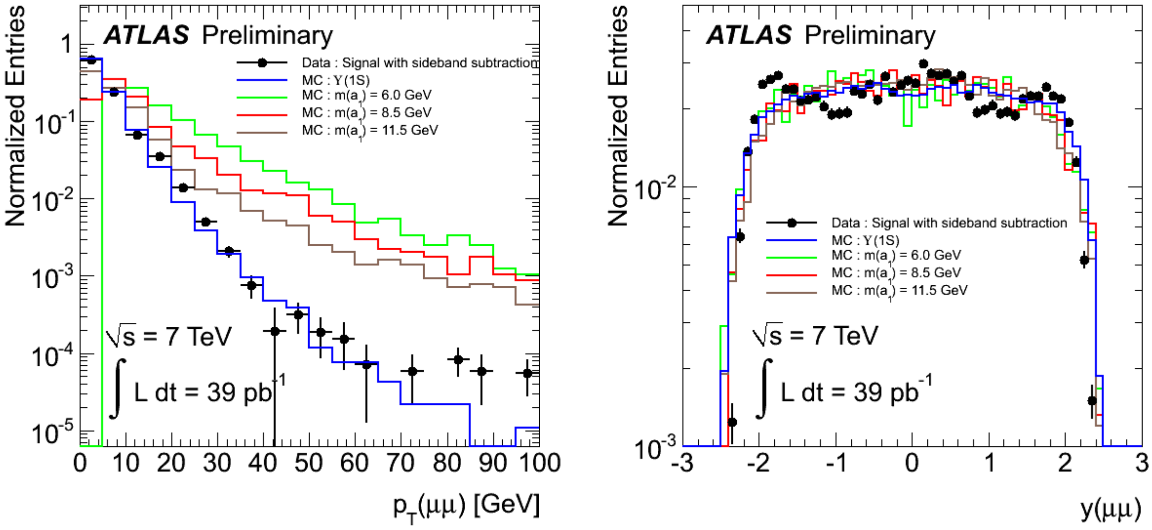

(a)

(b)

Figure 3: Distributions of dimuon (a) p_T, and (b) rapidity after the dimuon selection, for background-subtracted $\Upsilon(1S)$ data compared to predictions from $\Upsilon(1S)$ and a_1 simulation for several a_1 masses. Note that the a_1 MC has a generator-level cut of $p_T > 2.5$ GeV applied to each muon.

4.2 Likelihood Ratio Selections

In order to increase the significance of a potential $a_1 \to \mu^+\mu^-$ signal, background from muon pairs not coming from the decay of a single particle is reduced using a multi-variate discriminant – the $N \times 1D$ Likelihood Ratio. In the Likelihood Ratio method, the discriminating variable, $R \equiv (1 - Y)/(1 + Y)$, is constructed from the product, $Y \equiv \prod y_i$, with $y_i = f_{bkg}(x_i)/f_{sig}(x_i)$ the ratio of the likelihood to observe the variable, x_i, in the background ($f_{bkg}(x_i)$) and signal ($f_{sig}(x_i)$).

The following observables are used to construct R:

- χ^2/N_{dof} for the dimuon vertex fit;
- $E_T^{\mathrm{cone20}}/p_T(\mu_1)$: the transverse energy, measured in the calorimeters, in a cone of size $\Delta R = 0.20$ centered on the direction of the higher p_T muon, divided by the p_T of that muon. For this calculation, the expected muon energy loss in the calorimeters is subtracted from E_T^{cone20}.
- $E_T^{\mathrm{cone20}}/p_T(\mu_2)$: the same quantity for the lower p_T muon.

These observables exhibit good discrimination between signal and background and have minimal dependence on the a_1 mass.

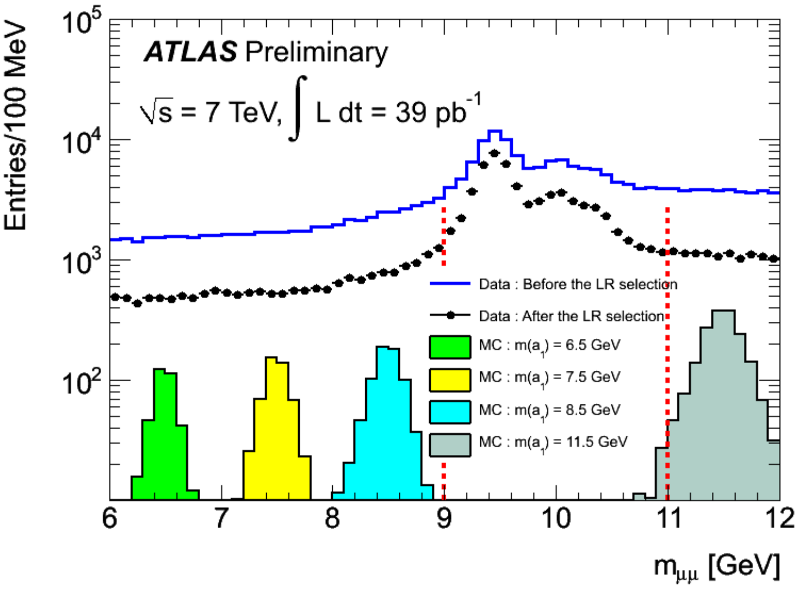

Figure 4: The $m_{\mu\mu}$ spectrum after the dimuon selection (open histogram), and after the Likelihood Ratio selection (points). Also shown are the predicted $a_1 \to \mu^+\mu^-$ spectra (with arbitrary normalization) for various a_1 masses.

Probability density functions (PDFs) used in the Likelihood Ratio are derived from data. The background PDF is extracted from distributions of the variables in the $m_{\mu\mu}$ sidebands 4.5 – 5.5 GeV and 12.5 – 14.0 GeV. These sidebands are chosen to be separated by 500 MeV from the lower and upper boundaries of the potential signal region (6 – 12 GeV) corresponding to approximately three times the average mass resolution in this region. The efficiency of the Likelihood Ratio selection changes by < 2% if background PDFs are constructed separately in three mass regions: 6.0–7.0, 7.0–9.0, and 11.0–12.0 GeV.

Signal PDFs are constructed from events around the Υ(1S) resonance (9.0 – 10.0 GeV). A fit is performed to the full mass range (6–12 GeV) without any a_1 contribution, as described in Section 5.2, to extract an estimate of the numbers of Υ(1S) and background events in the 9–10 GeV region. Distributions of the Likelihood Ratio variables are constructed in sideband region events (6.0–7.5 and 11.5–12.0 GeV), scaled to the background predicted under the Υ(1S) peak. These are then subtracted from the equivalent distributions in Υ(1S) region events (9.0–10.0 GeV) to obtain pure Υ(1S) PDFs. The background-subtracted distributions are used as an estimate of the true a_1 signal PDFs since distributions of the Likelihood Ratio variables are predicted to be similar for Υ(1S) and a_1 simulation as shown in Fig. 5. Predicted PDFs do not change appreciably with a_1 mass confirming that these variables are insensitive to the details of the resonance production mechanism.

Generally good agreement between background-subtracted data and Υ(1S) MC is observed in Fig. 5 except for some discrepancies in the tails of the distributions. These tails have a small effect on the overall efficiency. Nevertheless, modeling them with data gives a better approximation of the true Likelihood Ratio and hence is preferred to deriving the signal PDFs from simulation.

Sensitivity to a possible a_1 signal is enhanced by optimizing the cut on the variable, R, using $\varepsilon_{\mathrm{LR}}(a_1)/\sqrt{N_{bkg}}$ as the metric of optimization. In this calculation, the efficiency of the Likelihood Ratio selection for signal events, $\varepsilon_{\mathrm{LR}}(a_1)$, is determined from all events in the simulation of 7.5 GeV mass a_1 particles that pass the Likelihood Ratio selection. The number of background events under a potential signal, N_{bkg}, is predicted by extrapolating a fourth order polynomial fit to data in sideband regions to the signal region of ±3σ in mass resolution about 7.5 GeV.

Distributions of the values of the Likelihood Ratio, R, are shown in Fig. 6 for background (derived from sidebands) and for signal (derived from the simulation of 7.5 GeV mass a_1 particles). The mass spectrum for the final event sample, after application of the Likelihood Ratio cut, is shown in Fig. 4.

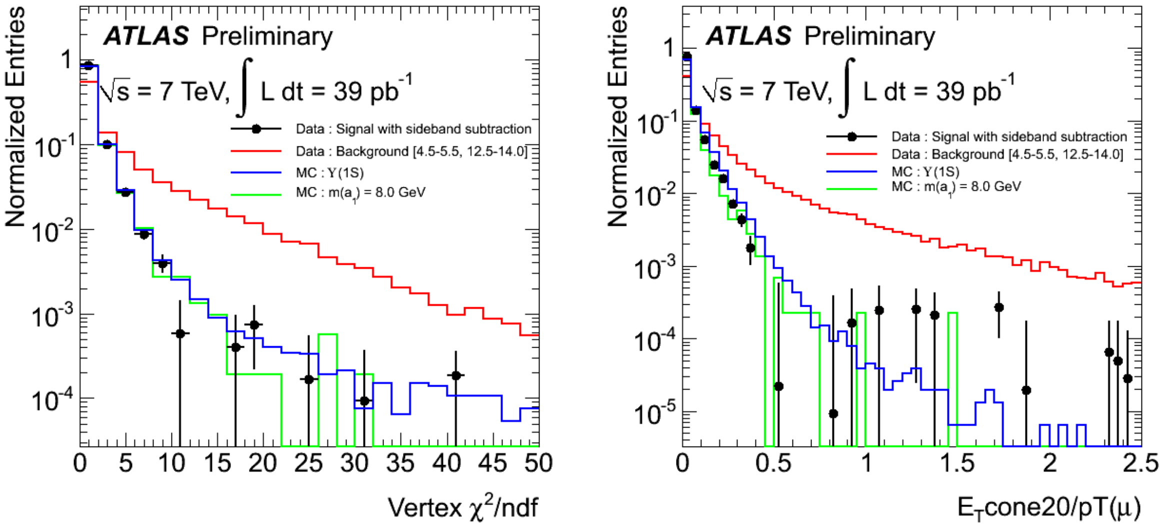

(a)

(b)

Figure 5: PDFs for variables used in constructing the Likelihood Ratio, for: signal (from background-subtracted $\Upsilon(1S)$ data); background (from data sidebands); and predictions from $\Upsilon(1S)$ MC, and a_1 MC (with $m(a_1)$=8.0 GeV). The Vertex χ^2 variable is shown in (a), while $E_T^{\text{cone20}}/p_T(\mu_{1,2})$ is shown in (b).

5 Cross-Section Limits

No evidence for a resonance, aside from the well known Υ states, is apparent in the final data sample (see Fig. 4). Therefore limits are set on the $gg \to a_1$ production cross section, $\sigma(gg \to a_1)$, times $a_1 \to \mu^+\mu^-$ branching fraction, $BR(a_1 \to \mu^+\mu^-)$:

$$\sigma(gg \to a_1) \cdot BR(a_1 \to \mu^+\mu^-) = \frac{N_{\text{sig}}^{95\%}}{\varepsilon\, \mathcal{L}} \tag{2}$$

In Eq. 2, $N_{\text{sig}}^{95\%}$ is the 95% confidence level limit on the number of $a_1 \to \mu^+\mu^-$ signal events for a given $m(a_1)$; ε is the total efficiency for observing an a_1 of that mass using the selection; and $\mathcal{L}$ is the integrated luminosity of the data sample, as discussed in Section 3.

5.1 Efficiency

The efficiency to select $a_1 \to \mu^+\mu^-$ decays is factorized into four components:

$$\varepsilon \;=\; \varepsilon_{\text{acc}} \;\cdot\; \varepsilon_{\mu\mu} \;\cdot\; \varepsilon_{\text{trig}} \;\cdot\; \varepsilon_{\text{LR}} \tag{3}$$

where ε_{acc} is the kinematic acceptance for the a_1, $\varepsilon_{\mu\mu}$ is the efficiency of the dimuon selection cuts, $\varepsilon_{\text{trig}}$ is the trigger efficiency, and ε_{LR} is the efficiency of the Likelihood Ratio selection. The efficiency for each component is calculated relative to all the previous selections.

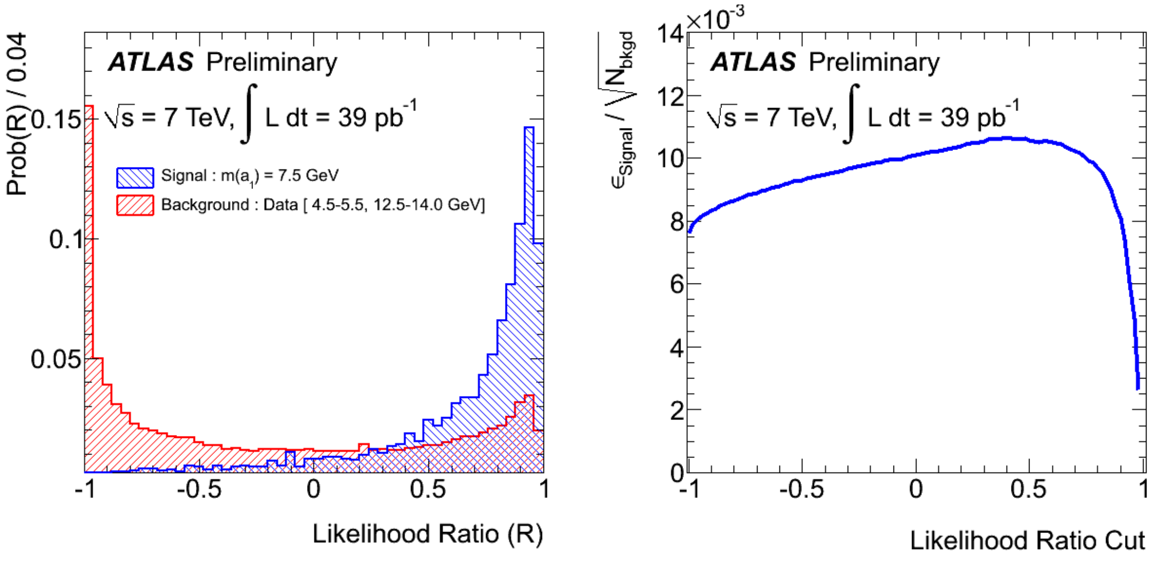

(a)

(b)

Figure 6: (a) Distributions of the Likelihood Ratio, R, expected for background (from sideband data) and signal (from 7.5 GeV a_1 MC). Also shown, (b), is the parameter $\varepsilon_{\rm LR}(a_1)/\sqrt{N_{bkg}}$ as a function of the value of the cut on R used in cut optimization.

The first three components ($\varepsilon_{\rm acc}$, $\varepsilon_{\mu\mu}$, and $\varepsilon_{\rm trig}$) are defined similarly to the corresponding efficiencies in Ref. [31]. Briefly, the kinematic acceptance, $\varepsilon_{\rm acc}$, measures the fraction of a_1 decays with transverse momentum, $p_{\rm T}$, and rapidity, y, that occur in the fiducial acceptance of the dimuon triggers used in this analysis. It is approximated by generator-level cuts of $p_{\rm T} > 4.0$ GeV and $|\eta| < 2.5$ for both muons.

The dimuon efficiency can be written:

$$\varepsilon_{\mu\mu} = \varepsilon_C(\mu^+)\varepsilon_{CT}(\mu^-) \; + \; \varepsilon_C(\mu^-)\varepsilon_{CT}(\mu^+) \; - \; \varepsilon_C(\mu^+)\varepsilon_C(\mu^-) \tag{4}$$

where ε_C and ε_{CT} refer to the efficiencies for reconstructing a *combined* muon and for observing a muon that is either reconstructed as *combined* or *tagged*. The individual terms are determined as a function of muon $p_{\rm T}$ and η from data using the "tag-and-probe" method [30, 31]. The total dimuon selection efficiency is the average of these $p_{\rm T}$ and η dependent efficiencies over the $a_1 \to \mu^+\mu^-$ spectrum predicted from MC at each a_1 mass point.

The efficiency of the dimuon trigger used to select data for this analysis is calculated as a function of dimuon opening angle, $\Delta R(\mu\mu)$, and rapidity, $y(\mu\mu)$, using Υ(1S) and J/ψ MC. Correction factors to these predictions are derived using data collected with a variety of non-muon triggers (mainly EM). $J/\psi \to \mu^+\mu^-$ and $\Upsilon(1S) \to \mu^+\mu^-$ candidates are reconstructed in this dataset and the efficiency of the dimuon trigger with respect to the offline muon selection is calculated in several bins of $\Delta R(\mu\mu)$ from the number of reconstructed J/ψ and Υ(1S) candidates that also fire the dimuon trigger. This data-based efficiency is then compared to that calculated using MC to derived the correction factors. Since these correction factors are consistent with a common mean, a single data-to-MC scale factor is used for all $\Delta R(\mu\mu)$ and $y(\mu\mu)$.

The Likelihood Ratio selection is unique to this analysis. Its efficiency is calculated, relative to the other selections, using simulated a_1 events input into the data-driven Likelihood Ratio estimator. As can be seen in Fig. 5, the simulation models the individual components of the ratio R quite well.

The individual efficiency values used in this calculation, along with their systematic errors (see Section 6) are shown in Fig. 7 as a function of $m(a_1)$.

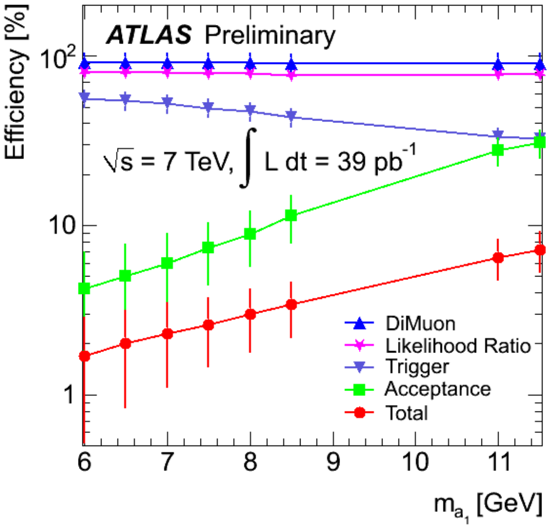

Figure 7: Values for the components entering the efficiency calculation (ε_{acc}, $\varepsilon_{\mu\mu}$, $\varepsilon_{\text{trig}}$, ε_{LR}, and ε) vs. $m(a_1)$. Note that the efficiencies shown here do not include effects of loss of signal near the mass region borders.

5.2 Limit Extraction Procedure

Limits on the number of signal events consistent with the data, $\mu(m(a_1))$, are derived using a profile likelihood method [33] as implemented in RooStats [34]. A test statistic

$$q_\mu \equiv -2\ln\lambda(\mu) = -2\ln\frac{L(\mu,\hat{\hat{\boldsymbol{\theta}}})}{L(\hat{\mu},\hat{\boldsymbol{\theta}})} \tag{5}$$

is used, where μ is the number of signal events, and $\boldsymbol{\theta}$ represents other (nuisance) parameters of the likelihood. The quantity in the numerator is calculated at the values, $\hat{\hat{\boldsymbol{\theta}}}$, that maximize it for a given μ. The quantity in the denominator represents the global maximum of the likelihood function, which occurs at parameters $(\hat{\mu},\hat{\boldsymbol{\theta}})$. This technique allows systematic effects due to uncertainties on the nuisance parameters to be included automatically in limits derived on μ.

The likelihood function is defined as the product over bins of width 50 MeV in $m_{\mu\mu}$:

$$L(\mu,\vec{\theta}) = \prod_{i=\text{bin}} \frac{\eta_i^{N_i}}{N_i!}\, e^{-\eta_i} \tag{6}$$

where N_i is the number of events observed in bin i; and the predicted number of events in that bin is given by:

$$\begin{aligned}\eta_i &= \mu f_{s,i}(m(a_1),\sigma_m) + n_b f_{b,i}(\boldsymbol{p}_b)\\ &+ n_{1S} f_{1S,i}(m_{1S},\sigma_{1S}) + n_{2S} f_{2S,i}(m_{2S},\sigma_{2S}) + n_{3S} f_{3S,i}(m_{3S},\sigma_{3S})\end{aligned} \tag{7}$$

Probability density functions ($f_{x,i}$) for signal and background are evaluated at the center of each bin.

The PDFs for an a_1 signal at mass $m(a_1)$ (f_s) and for the three Υ peaks ($f_{1S,2S,3S}$) are approximated by double Gaussians with means fixed to the a_1 mass in question, and to the world-average values [35] for the Υ resonances, respectively. Yields of each of these sources ($\mu, n_{1S}, n_{2S}, n_{3S}$) are free to float in the fits. The widths of the a_1 and Υ resonances are entirely dominated by detector resolution, which scales linearly with resonance mass for these two-track decays. Therefore the widths and relative fractions of the two Gaussians describing the $\Upsilon(1S)$ are allowed to float freely in the fit, but the widths of all the other resonances in the fit are constrained to these $\Upsilon(1S)$ values using the linear relationship derived from MC. Finally, the background PDF (f_b) is modeled by a fourth-order polynomial with floating coefficients ($p_{0,1,2,3}$) and yield (n_b).

Fits are performed in two mass regions (6–11 GeV and 9–12 GeV) because the different composition of the background in these two regions complicates modeling it over the full region using a simple function. Results of fits assuming no a_1 signal are shown in Fig. 8. Parameters extracted from the fits related to the Υ resonances are consistent between the two regions.

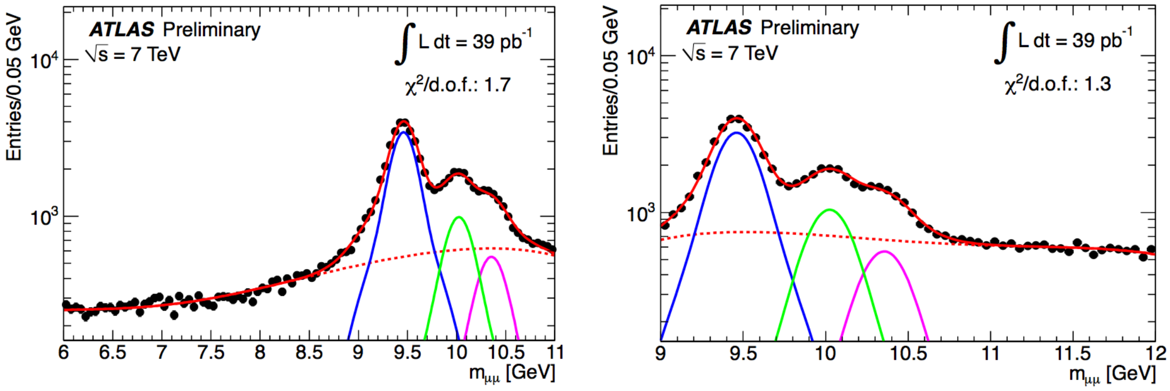

(a)

(b)

Figure 8: Results of background-only fits in the (a) low- and (b) high-mass regions. The blue, green, and magenta curves correspond to the Υ 1S, 2S, and 3S predictions from the fit, while the dashed red curve represents the fitted background.

6 Systematic Uncertainties

Several sources of systematic uncertainty affect the cross section limit calculation. Uncertainties on the nuisance parameters are included implicitly in the limit on μ by the profile likelihood method itself. However, uncertainties affecting the luminosity and efficiency calculations are dealt with by adjusting the efficiency used in the cross section calculation downward by one standard deviation from its central value. This one standard deviation fluctuation is obtained by summing in quadrature the individual components of the luminosity and efficiency systematics described below.

1. **Luminosity:** The updated ATLAS luminosity uncertainty of 3.4% [36] is used.

2. **Acceptance:** Sources of uncertainty in the calculation of the acceptance include those arising from modeling of initial and final state radiation (ISR/FSR); from the choice of parton density functions; from the choice of α_S; and from knowledge of effects beyond Next-to-Leading Order (NLO) in the production model. The calculated acceptance is particularly sensitive to the a_1 production model assumed in the simulation because of the $p_T > 4$ GeV cut on the two muons. Especially in the low a_1 mass region ($m(a_1) < 8$ GeV), only those events with substantial radiation can produce a_1 particles with sufficient transverse boosts to allow muons from their decays to pass the acceptance cuts. Detailed studies of each of the individual effects listed above are being performed, but for

this preliminary result, the acceptance systematic is estimated as half the difference between the acceptances calculated using the default MC@NLO simulation and a Pythia simulation of these events. The MC@NLO and Pythia simulations considered use different ISR/FSR models, different PDFs, and different values of α_S. The Pythia model generates hard scattering events at Leading Order (LO), in contrast to MC@NLO, which uses full NLO matrix elements. Pythia then models gluon radiation using a parton shower. Thus, differences between the two simulations, which come mainly from their treatment of gluon radiation, are expected to be significantly larger than those that would occur from a true comparison of NLO to Next-to-NLO effects. Until such a comparison exists, the acceptance systematic estimated by comparing LO + parton shower (Pythia) to NLO production (MC@NLO) is a conservative upper bound on the true uncertainty.

3. **Dimuon reconstruction efficiency:** This systematic is based mainly on the statistics of the tag-and-probe data sample used to derive the individual efficiencies $[\varepsilon_{CT}(\mu), \varepsilon_{CT}(\mu)]$ in their p_T and η bins. Values in all bins are varied coherently by $+1\sigma$ or -1σ and the resulting $\varepsilon_{\mu\mu}$ is used in the calculation of the total efficiency.

4. **Trigger efficiency:** Systematics on the estimate of the trigger efficiency arise from the statistics of the MC sample used to construct the efficiency maps and from the uncertainty on the data-based correction factor. The latter is derived from the statistics of the non-muon trigger control sample.

5. **Likelihood Ratio selection:** Several sources of potential systematic uncertainty in the Likelihood Ratio selection have been considered. The data-based PDFs used to construct R are varied within their statistical uncertainties in a series of toy MC experiments and the spread in the efficiencies obtained in each pseudo-experiment is calculated. This leads to systematic differences in $\varepsilon_{\mathrm{LR}}$ of less than 1%. Differences between the distributions of Likelihood Ratio variables in $\Upsilon(1S)$ and a_1 simulation give changes in $\varepsilon_{\mathrm{LR}}$ that are <1%. Statistics of the a_1 MC sample used as the basis of the Likelihood Ratio efficiency estimate could also contribute to the total systematic error. However, this uncertainty is <1% for all masses and is therefore neglected. A larger systematic effect comes from differences between $\Upsilon(1S)$ data and simulation. The size of this difference is estimated by extracting the number of $\Upsilon(1S)$ events in data using fits to the $m_{\mu\mu}$ mass spectra before and after the Likelihood Ratio selection. The efficiency calculated from this data-driven method differs from that found in $\Upsilon(1S)$ MC by 3%, which is assigned as a systematic error due to modeling of the Likelihood Ratio efficiency.

The magnitudes of each of these uncertainties as a function of $m(a_1)$ are listed in Table 1.

7 Results and Conclusions

Figure 9 shows the result of the limit calculation as a function of dimuon mass, taking into account the systematic effects described in Section 6. In this figure, limits on μ are translated to limits on the a_1 cross section times branching ratio using Eq. 2. The observed limit (black line in Fig. 9) is presented as a 16% power constrained limit (PCL) and uses an asymptotic expression for q_μ [33]. Note that the observed limit increases at the edges of the mass regions because a potential signal is cut off at the boundaries.

The statistical nature of the fluctuations in the cross section upper limit is studied by generating 500 statistically independent pseudo-data samples based on the fitted $m_{\mu\mu}$ distribution with the a_1 signal excluded. For each pseudo-experiment, a binned $m_{\mu\mu}$ distribution is generated with each bin's contents drawn randomly from a Poisson distribution based on the prediction of the background-only fit in that bin. The limit setting procedure is repeated for each pseudo-experiment, and the median limit and its one- and two-standard deviation bounds are extracted. This expected limit, with its $\pm1\sigma$ and $+2\sigma$ bands, is shown

Table 1: Systematic uncertainties affecting this analysis. The total uncertainty is obtained by adding the individual effects in quadrature.

	Relative Uncertainty (%) at $m(a_1)$ (GeV)							
Source	6.0	6.5	7.0	7.5	8.0	8.5	11.0	11.5
Luminosity	±3							
Pythia vs MC@NLO	±67	±55	±49	±40	±36	±32	±20	±20
Dimuon Efficiency	$^{+14}_{-13}$	$^{+14}_{-13}$	$^{+14}_{-13}$	$^{+14}_{-13}$	$^{+14}_{-13}$	$^{+14}_{-13}$	$^{+15}_{-14}$	$^{+15}_{-14}$
Trigger Correction	±8							
MC Statistics	±10	±10	±10	±10	±10	±10	±9	±9
Likelihood Ratio Modeling	±3							
Total (Pythia vs MC@NLO)	±70	±59	±53	±45	±41	±37	±28	±28

in Fig. 9. The -2σ band is not displayed because it systematically goes to zero in this method. Deviations of the observed limit from its expected values are consistent with statistical fluctuations arising from a null-signal $m_{\mu\mu}$ distribution taking into account *look-elsewhere* effects. Using the techniques described in Ref. [37], probabilities of observing a given fluctuation are increased by factors of 70–90 (depending on the precise mass at which the fluctuation occurs) over what would be calculated were an a_1 particle to exist at known mass due to the fact that the fluctuation could occur *anywhere* in the mass range.

In conclusion, a search for a light CP-odd Higgs (a_1) predicted in the NMSSM has been performed. No evidence for this state is observed and upper limits are set on its production cross section times muonic branching ratio, $\sigma(gg \to a_1) \cdot BR(a_1 \to \mu^+\mu^-)$, in the a_1 mass ranges 6–9 GeV and 11–12 GeV. Because the result is quoted in terms of a cross section times branching ratio, it does not depend on NMSSM assumptions. However, within that model these limits will constrain regions with high $\tan\beta$ and small CP-odd Higgs boson mixing angle, $\cos\theta_A \approx 1$.

References

[1] G. L. Kane et al., *Study of Constrained Minimal Supersymmetry*, Phys. Rev. D **49** 6173 (1994) .

[2] R. Barate et al., *Search for the Standard Model Higgs boson at LEP*, Phys. Lett. B **565** 61, [arXiv:hep-ex/0306033] (2003) .

[3] M. Maniatis, *The NMSSM reviewed*, [arXiv:hep-ph/0906.0777v1] (2009) .

[4] J. Gunion, *A light CP-odd Higgs boson and the muon anomalous magnetic moment*, JHEP **0908** 032, [arXiv:hep-ph/0808.2509v1] (2008) .

[5] M. A. Sanchis-Lozano, *Searching for new physics in leptonic decays of bottomonium*, Mod. Phys. Lett. A **17** 2265, [arXiv:hep-ph/0206156] (2002) .

[6] M. A. Sanchis-Lozano, *Leptonic universality breaking in Upsilon decays as a probe of new physics*, Int. J. Mod. Phys. A **19** 2183 [arXiv:hep-ph/0307313] (2004) .

[7] Y.-J. Zhang and H.-S. Shao, *Leptonic Decay of Upsilon, a Possible Signature of New Physics*, [arXiv:0911.1766v1] (2009) .

[8] BaBar Collab., *Test of lepton universality in Upsilon(1S) decays at BaBar*, Phys. Rev. Lett. **104** 191801, [arXiv:1002.4358v2] (2010) .

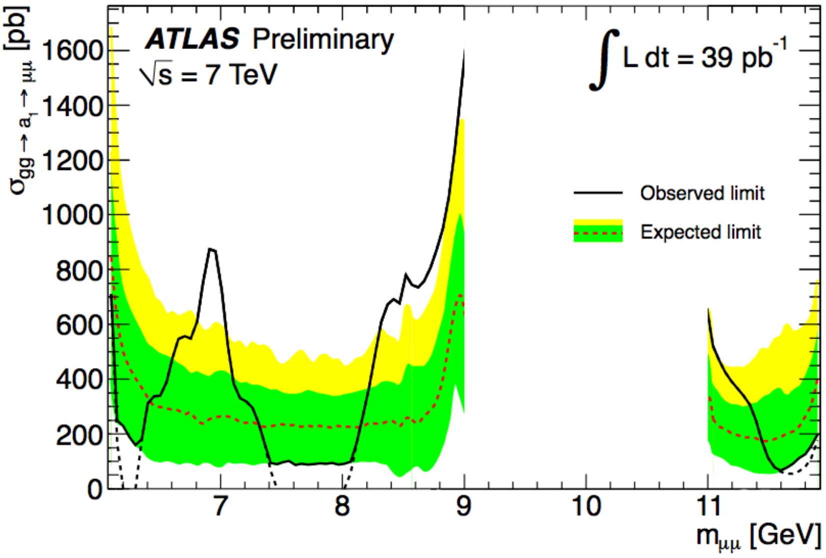

Figure 9: Upper limits on $\sigma(gg \to a_1) \cdot BR(a_1 \to \mu^+\mu^-)$ at 95% confidence level. The black solid line is the observed upper limit, presented as a 16% power constrained limit using asymptotic formulas, while the dashed red line corresponds to the expected limit, assuming absence of a signal. The green/yellow areas represent the $\pm 1\sigma / +2\sigma$ uncertainties on the expected limit. The -2σ band is not displayed because it systematically goes to zero in this method.

[9] J. Gunion, D. Hooper, and B. McElrath, *Light Neutralino Dark Matter in the NMSSM*, Phys. Rev. D **73** 015011, [arXiv:hep-ph/0509024] (2005) .

[10] R. Dermisek and J. Gunion, *Many Light Higgs Bosons in the NMSSM*, Phys. Rev. D **79** 055014, [arXiv:hep-ph/0811.3537v1] (2008) .

[11] A. Akeroyd, A. Arhrib, and Q.-S. Yan, *Charged Higgs bosons in the Next-to MSSM (NMSSM)*, Eur. Phys. J. C **55** 653-665, [arXiv:hep-ph/0712.3933v2] (2008) .

[12] R. Dermisek and J. Gunion, *The NMSSM Solution to the Fine-Tuning Problem, Precision Electroweak Constraints and the Largest LEP Higgs Event Excess*, Phys. Rev. D **76** 095006, [arXiv:0705.4387] (2007) .

[13] R. Dermisek and J. Gunion, *Direct production of a light CP-odd Higgs boson at the Tevatron and LHC*, Phys. Rev. D **81** 055001, [arXiv:0911.2460v1] (2009) .

[14] BaBar Collab., *Search for Dimuon Decays of a Light Scalar Boson in Radiative Transitions* $\Upsilon \to \gamma A_0$, Phys. Rev. Lett. **103** 081803, [arXiv:hep-ph/0905.4539v1] (2009) .

[15] D0 Collab., *Search for NMSSM Higgs bosons in the* $h \to aa \to 4\mu, 2\mu 2\tau$ *channels using* $p\bar{p}$ *collisions at* $\sqrt{s}$ = *1.96 TeV*, Rev. Lett. **103** 061801, [arXiv:0905.3381] (2009) .

[16] R. Dermisek and J. Gunion, *New constraints on a light CP-odd Higgs boson and related NMSSM Ideal Higgs Scenarios*, Phys. Rev. D **81** 075003, [arXiv:1002.1971v1] (2010) .

[17] A. Belyaev, J. Pivarski, S. Senkin, and A. Tatarinov, *LHC discovery potential of the lightest NMSSM Higgs in the* $h_1 \to a_1 a_1 \to$ *4 muons channel*, Phys. Rev. D **81** 075021, [arXiv:1002.1956v1] (2010) .

[18] ALEPH Collab., *Search for neutral Higgs bosons decaying into four taus at LEP2*, [arXiv:1003.0705v1] (2010) .

[19] CDF Collab., *Search for NMSSM Higgs in Top Quark Decays*, [http://www-cdf.fnal.gov/physics/new/top/2009/tprop/nMSSMhiggs/] (2010) .

[20] E. Fullana and M.-A. Sanchis-Lozano, *Hunting a light CP-odd non-standard Higgs boson through its tauonic decay at a (Super) B factory*, Phys. Lett. B **653** 67 [arXiv:hep-ph/0702190] (2007) .

[21] F. Domingo, U. Ellwanger, E. Fullana, C. Hugonie, and M. A. Sanchis-Lozano, *Radiative Upsilon decays and a light pseudoscalar Higgs in the NMSSM*, JHEP **0901** 061 [arXiv:0810.4736] (2009) .

[22] M. A. Sanchis-Lozano, *Comment on 'New constraints of a light CP-odd Higgs boson and related NMSSM Ideal Higgs Scenarios' by Dermisek and Gunion (arXiv:1002.1971 [hep-ph])*, [arXiv:1003.0312] (2010) .

[23] ATLAS Collab., *The ATLAS Experiment at the CERN Large Hadron Collider*, JINST 3 S08003 (2008) .

[24] ATLAS Collab., *ATLAS Monte Carlo tunes for MC09*, Tech. Rep. ATL-PHYS-PUB-2010-002, ATL-PHYS-PUB-2010-033 (2010) .

[25] S. Frixione and B. Webber, *Matching NLO QCD computations and parton shower simulations*, JHEP 0206 (2002) 029 [arXiv:hep-ph/0204244] (2002) .

[26] J. Pumplin, D. R. Stump, J. Huston, H. L. Lai, P. M. Nadolsky and W. K. Tung, *New generation of parton distributions with uncertainties from global QCD analysis*, JHEP **0207**, 012 [arXiv:hep-ph/0201195] (2002) .

[27] T. Sjostrand, S. Mrenna, and P. Z. Skands, *PYTHIA 6.4 Physics and Manual*, JHEP 05 (2006) 026 [arXiv:hep-ph/0603175] (2006) .

[28] A. Sherstnev and R. S. Thorne, *Parton Distributions for LO Generators*, Eur. Phys. J. C **55**, 553 (2008) .

[29] S. Agostinelli et al., *Geant4: A simulation toolkit*, Nucl. Instrum. Meth. A **506** 3 250-303 (2003) .

[30] ATLAS Collab., *Determination of the muon reconstruction efficiency in ATLAS at the Z resonance in proton-proton collisons at* $\sqrt{s} = 7$ *TeV*, ATLAS-CONF-2011-008 (2011) .

[31] ATLAS Collab., *Measurements of the prompt and non-prompt differential production cross-sections of* $J/\psi \to \mu^+\mu^-$ *in proton-proton collisions at* $\sqrt{s} = 7$ *TeV*, ATLAS-BPHYS-2010-01-002 (2011) .

[32] V. Kostyukhin, *VKalVrt - a package for vertex reconstruction in ATLAS*, ATLAS-PHYS-2003-031 (2003) .

[33] G. Cowan, K. Cranmer, E. Gross, and O. Vitells, *Asymptotic formulae for likelihood-based tests of new physics*, accepted by Eur. Phys. J. C [arXiv:1007.1727v2] (2010) .

[34] [https://twiki.cern.ch/twiki/bin/view/RooStats/WebHome] .

[35] C. Amsler et al., *Review of Particle Physics*, Phys. Lett. B **667** 1 (2008) .

[36] ATLAS Collab., *Updated Luminosity Determination in pp Collisions at $\sqrt{s}$ = 7 TeV using the ATLAS Detector*, ATLAS-CONF-2011-011 (2011) .

[37] E. Gross and O. Vitells, *Trial factors for the look elsewhere effect in high energy physics*, [arXiv:1005.1891] (2010) .